Generalized Travel-Time Inversion on Unstructured Grids

Vegard R. Stenerud [*,1]

Department of Mathematical Sciences, NTNU, NO–7491 Trondheim, Norway

Knut–Andreas Lie [2]

Department of Applied Mathematics, SINTEF, P.O. Box 124 Blindern, NO–0314 Oslo, Norway

Vegard Kippe [2]

Department of Applied Mathematics, SINTEF, Oslo, Norway (Currently at StatoilHydro, Bergen, Norway)

Abstract

We propose an extension to general unstructured grids for the so-called generalized travel-time inversion method for inversion of production data. The framework of the inversion method applies directly to general unstructured grids, but there are aspects regarding sensitivities and regularization that have to be addressed. First, we propose a generalized smoothing operator for the regularization to impose smooth modification on reservoir parameters. Second, to handle reservoir models with great heterogeneity in cell sizes, we investigate the use of rescaled sensitivities (average cell volume multiplied by local sensitivity density) in the inversion.

We demonstrate the utility of our extensions by three numerical examples. First, we validate the inversion method by applying it to a reservoir model represented both on a Cartesian and on a refined triangular grid. Second, we apply the method for a highly unstructured grid with large differences in cell sizes. Finally, we consider an example with faults and non-neighboring connections. All examples show that our method is able to match the data with the same quality as has been obtained earlier on structured grids and without degrading the realism of the reservoir parameters.

Key words: History matching, Streamlines, Unstructured grids, Permeability

1 Introduction

The *generalized travel-time* (GTT) inversion method was introduced by Vasco et al. (1999) and He et al. (2002) and has been successfully applied to several field cases; see e.g., Qassab et al. (2003) and Hohl et al. (2006). Although the inversion method itself does not require a streamline simulator (Cheng et al., 2005b), it is most efficient if the required production-response sensitivities are approximated by analytical integrals streamlines and a streamline simulator is used for the forward simulation. However, the inversion method can be implemented on top of any simulator on a Cartesian grid that outputs velocity fields during the forward simulation (Cheng et al., 2005b). In this paper we discuss how to extend the GTT inversion method to general unstructured grids.

Although the framework of the inversion method in principle can be generalized to unstructured grids, the method has not yet been applied to general unstructured grids in practice, and there are issues to address regarding regularization and the use of sensitivities. First, the smoothing operator involved in the regularization has to be generalized to unstructured grids. For moderately skewed, logically Cartesian grids, finite-difference approximations for the Laplacian is used to measure the smoothness. The key question is therefore whether this stencil is directly generalizable or if one has to introduce some sort of spatial weighting. Second, the computation of production-response sensitivities on unstructured grids has to be investigated and verified. In addition, non-neighboring connections that can occur in connection with faults and general unstructured grids have to be addressed.

In two recent papers (Stenerud et al., to appear,s) we proposed to combine GTT inversion with a highly efficient multiscale-streamline solver on Cartesian grids. In particular, we demonstrated how the sensitivities from the inversion method can be used to make certain simplifications in the multiscale flow solver in regions of low sensitivity, thereby reducing the total simulation time considerably with negligible loss in accuracy compared with a standard finite-difference simulator. The underlying multiscale mixed finite-element formulation (Chen and Hou, 2002; Aarnes, 2004) has later been extended as a very efficient flow solver for highly heterogeneous reservoirs on unstructured

* Corresponding author. Fax: +47 73593524
   Email addresses: `vegarste@math.ntnu.no` (Vegard R. Stenerud),
`Knut-Andreas.Lie@sintef.no` (Knut–Andreas Lie).
   URLs: `http://www.math.ntnu.no/~vegarste` (Vegard R. Stenerud),
`http://folk.uio.no/kalie` (Knut–Andreas Lie).

grids (Aarnes et al., to appear). We are confident that the combination of a multiscale-streamline simulator and sensitivity-based work-reduction strategy of (Stenerud et al., to appear) can easily be extended to unstructured grids, thereby giving significant speedup of the forward simulations. Herein, however, we only use a standard mixed finite-element method (MFEM) as our flow solver. Moreover, we implicitly assume that the grid has adequate mesh quality to provide forward simulations of sufficient accuracy. Mesh quality is often determined by the smallest angles in the grid and a grid with quite equilateral cells therefore indicates good mesh quality. Hence, grids with high mesh quality can still have large differences in cell sizes, used to refine important regions of the reservoir, for instance in the near-well regions or near channels, flow barriers, etc.

The outline of the paper is as follows: First, we present the forward model and the inversion method and describe how to compute analytical approximations to the sensitivities. Then, we propose smoothing operators which are intended to be robust and avoid grid effects for general unstructured 3-D grids with large differences in cell sizes. Finally, the applicability of our method is discussed in terms of a few numerical examples. In particular, we compare the new smoothing operator(s) with the standard finite-difference approximations for the Laplacian. In addition, we address aspects related to grid heterogeneity, sensitivities, robustness, and non-neighboring connections. For simplicity, we only consider two-dimensional triangular and quadrilateral grids.

2 Flow Model

We consider incompressible two-phase flow of oil and water in a non-deformable and permeable medium. For simplicity, we neglect the effects of gravity, compressibility, and capillary forces and assume no-flow boundary conditions. Our flow model then consists of an elliptic pressure equation

$$\nabla \cdot \vec{u} = q_t, \quad \vec{u} = -\lambda_t(S) K \nabla p, \tag{1}$$

and a quasilinear hyperbolic transport equation

$$\phi \frac{\partial S}{\partial t} + \nabla \cdot (f_w(S)\vec{u}) = q_w. \tag{2}$$

The primary unknowns in the coupled system (1)–(2) are the pressure p, the total Darcy velocity $\vec{u}$, and the water saturation S. The underlying porous rock formation is modeled in terms of the absolute permeability K and the porosity ϕ, which henceforth are assumed to depend on the spatial variable

only. Further, q_t and q_w represent fluid sources and sinks (e.g., injection and production wells). Finally, $\lambda_t = \lambda_w + \lambda_o$ denotes the total mobility, where the mobility λ_j of each phase $(j = o, w)$ is given as the relative permeability k_{rj} divided by the phase viscosity μ_j, and $f_w = \lambda_w/\lambda_t$ is the fractional-flow function of water.

By making a coordinate transformation, the three-dimensional transport equation can be decoupled into a family of one-dimensional transport equations. Rather than using the arc length along the streamline as a spatial coordinate, we use the time-of-flight defined by,

$$\tau = \int_\Sigma \frac{\phi(\xi)}{|\vec{u}(\xi)|} \, d\xi =: \int_\Sigma s(\xi) \, d\xi,$$

where Σ denotes the streamline trajectory and s denotes the so-called slowness function $\phi/|\vec{u}|$. The operator identity $\vec{u} \cdot \nabla = \phi\frac{\partial}{\partial \tau}$ together with the incompressibility condition $\nabla \cdot \vec{u} = 0$ can be used to rewrite (2) as a family of one-dimensional transport equations along streamlines

$$\frac{\partial S}{\partial t} + \frac{\partial f_w}{\partial \tau} = 0. \tag{3}$$

The solution of (2) is obtained by tracing a set of streamlines, mapping the initial saturations from the 3-D pressure grid to 1-D streamlines, and then solving (3) along each streamline forward in time. Afterwards, the new streamline saturations are mapped (or averaged) back to the underlying 3-D grid to update mobilities before the pressure equation (1) is solved to recompute the pressure and velocity field. This solution process continues forward in time, alternating between a pressure step and a transport step for fluid saturation.

3 The Inversion Method

The heart of the inversion method is to determine perturbations $\delta\mathbf{m}$ that minimize the following function on a given simulation grid

$$\arg\min_{\delta\mathbf{m}} \ \|\delta\mathbf{d} - \mathbf{G}\delta\mathbf{m}\| + \underbrace{\beta_1\|\delta\mathbf{m}\|}_{\text{norm}} + \underbrace{\beta_2\|\mathbf{L}\,\delta\mathbf{m}\|}_{\text{smoothing}}. \tag{4}$$

The first term of (4) is the data-misfit term, where $\mathbf{d}$ denotes the observed data points, $\mathbf{m}$ the reservoir parameters, and $\mathbf{G} = \{\frac{\partial d_j}{\partial m_i}\}$ is the sensitivity matrix. The other two terms are regularization terms used to stabilize the under-determined inversion problem and β_1 and β_2 are scalars used to weight

the importance of each regularization term. The norm constraint $\|\delta\mathbf{m}\|$ measures the magnitude of $\delta\mathbf{m}$ and seeks to minimize the modifications made to the reservoir parameter $\mathbf{m}$. In the last term, $\mathbf{L}$ is a smoothing operator that measures the local roughness of $\delta\mathbf{m}$. This term therefore tends to keep the modifications made to the reservoir parameter $\mathbf{m}$ as smooth as possible. In other words, changes in the reservoir parameters are induced by size and sign of the data shifts $\delta\mathbf{d}$ and the magnitude and distribution of sensitivities $\mathbf{G}$, diminished by the norm regularization, and smeared out by the smoothing term.

A minimum for (4) can be obtained by a least-square solution of the augmented linear system

$$
\begin{bmatrix} \mathbf{G} \\ \beta_1\mathbf{I} \\ \beta_2\mathbf{L} \end{bmatrix} \delta\mathbf{m} = \begin{bmatrix} \delta\mathbf{d} \\ \mathbf{0} \\ \mathbf{0} \end{bmatrix}.
\tag{5}
$$

This system is typically solved with the iterative least-square minimization algorithm, LSQR (Paige and Saunders, 1982). This minimization method has proven to be robust and applicable for permeability fields on non-deformable logically Cartesian grids; see e.g., Qassab et al. (2003) and Hohl et al. (2006). Even though each grid cell in a logically Cartesian grid is identified by an ijk-triple, it is often convenient to give the grid cells a natural numbering $\mathcal{G} = \{1, 2, \ldots, N\}$. Hence, the framework can be applied directly to general unstructured grids (e.g., triangular or tetrahedral grids). However, as mentioned above there are issues to rule out to verify the applicability for general unstructured grids.

3.1 Quantification of Data Misfit

Misfit in dynamic data is commonly represented by a least-squares functional of the form:

$$
E = \sum_{k=1}^{N_w} \sum_{j=1}^{N_d^k} w_{kj} \left[y_k^{\text{obs}}(t_j^k) - y_k^{\text{calc}}(t_j^k) \right]^2.
\tag{6}
$$

Here y_k^{obs} and y_k^{calc} are the observed and calculated production responses in well k at time t_j^k; N_w and N_d^k denote the number of wells and the number of observed data per well, respectively; and w_{kj} represent data weights. The production responses can for instance be dynamic pressure, water cut, and/or gas-oil ratio. Henceforth we only consider water cut data.

Rather than minimizing (6) directly, we will use a one-step generalized travel-time (GTT) inversion (He et al., 2002), for which we seek a set of time-shifts $\Delta\mathbf{t} = \{\Delta t_k\}$ for the calculated production responses. A time-shift simply expresses how much a calculated production curve should be shifted in time to maximize the cross-correlation with the observed curve. To determine the optimal time-shifts, we minimize the following misfit at each well:

$$E_k(\Delta t_k) = \sum_{j=1}^{N_d^k} \left[y_k^{\mathrm{obs}}(t_j^k + \Delta t_k) - y_k^{\mathrm{calc}}(t_j^k) \right]^2. \tag{7}$$

Using the GTT inversion, we can match multiple data points as in amplitude inversion, while retaining the attractive quasilinear properties of travel-time inversion (Cheng et al., 2005a). We emphasize that computing time-shifts does not require new flow simulations, but can be done using data from the single forward simulation used to evaluate the data mismatch.

In practice, we do not use (7) directly. Instead we maximize the coefficient of determination:

$$R_k^2(\Delta t_k) = 1 - \frac{\sum_{j=1}^{N_d^k} \left[y_k^{\mathrm{obs}}(t_j^k + \Delta t_k) - y_k^{\mathrm{calc}}(t_j^k) \right]^2}{\sum_{j=1}^{N_d^k} \left[y_k^{\mathrm{obs}}(t_j^k) - \overline{y_k^{\mathrm{obs}}} \right]^2}, \tag{8}$$

where $\overline{y_k^{\mathrm{obs}}}$ is the average over all N_d^k data points at well k. Having determined the optimal time-shifts $\Delta\mathbf{t}$, the next step is to propagate them into changes in the reservoir parameters. For this we apply (5) with $\delta\mathbf{d} = \Delta\mathbf{t}$.

Finally, to measure the misfit in water cut during the inversion process we will use the amplitude and time-shift residuals ($w_{kj} = 1$ in (6))

$$E_{\mathrm{amplitude}} = \sqrt{E}, \qquad E_{\mathrm{time-shift}} = \left(\sum_{k=1}^{N} (\Delta t_k)^2 \right)^{1/2}.$$

3.2   Sensitivities on Unstructured Grids

For the sake of completeness, we briefly describe the analytical calculation of streamline-based approximate sensitivities. To this end, we consider a perturbation $\delta\mathbf{m}$ in the reservoir parameters, which will result in a time-shift δt in the calculated production curve for a given well. Thus, for each observation we have that (Vasco et al., 1999; He et al., 2002)

$$\delta t = \delta t_j = \left[\frac{\partial t_j}{\partial\mathbf{m}} \right] \cdot \delta\mathbf{m}. \tag{9}$$

Summing this equation over all data points N_d, we obtain an expression for the overall time-shift δt of the calculated production curve. By convention, $\Delta t = -\delta t$ (see (7)) and the sensitivity of the shift in the generalized travel time Δt with respect to reservoir parameter m_i is given by

$$\frac{\partial \Delta t}{\partial m_i} = -\frac{1}{N_d} \sum_{j=1}^{N_d} \frac{\partial t_j}{\partial m_i}. \tag{10}$$

Production data are calculated by averaging the flow rates of each connected streamline. Now we fix the water cut y_k^{calc} and the fractional flow contributions from each streamline. Then, by assuming a Buckley–Leverett profile along each streamline, the fractional flow at the outlet can be related to the streamline time-of-flight using the expression $\tilde{f}'_w(S_{o,\ell}) = \tau_\ell/t_j$, where $\tilde{f}_w$ is the convex hull of f_w and $S_{o,\ell}$ is the saturation at the outlet of streamline ℓ. Since $\tilde{f}'_w(S_{o,\ell})$ is fixed, it follows that $\partial t_j/\partial m_i$ is proportional to the sensitivity of the time-of-flight, which can be computed analytically from a single streamline simulation under the assumption that the streamlines do not shift because of small perturbations in reservoir properties. For example, the sensitivity of τ_ℓ with respect to permeability K_i in cell i is given by

$$\frac{\partial \tau_\ell}{\partial K_i} = \frac{\partial \Delta \tau_{\ell,i}}{\partial K_i} = \int_{\Sigma_{\ell,i}} \frac{\partial s(\xi)}{\partial K_i} \, d\xi = -\int_{\Sigma_{\ell,i}} \frac{s(\xi)}{K_i} \, d\xi = -\frac{\Delta \tau_{\ell,i}}{K_i}, \tag{11}$$

where the integral is along the streamline trajectory $\Sigma_{\ell,i}$ through cell i and $\Delta \tau_{\ell,i}$ is the associated incremental time-of-flight. Because the sensitivities are simple integrals along streamlines, the computation time scales very favorably with respect to the number of grid cells, thus making streamline-based sensitivities the preferred approach for integrating dynamic data into highly-detailed subsurface models.

As seen above, the parameter sensitivities in $\mathbf{G}$ can be computed as analytical integrals along streamlines and be obtained by post-processing output from a single flow simulation As such, the sensitivities are independent of the underlying grid geometry, which is accounted for in the tracing process. In the current paper, the tracing is performed by subdividing general polyhedral cells into triangles in 2-D and tetrahedra in 3-D and then computing the incremental streamline path analytically on each subcell. The sensitivity for an aggregated cell consisting of a collection of subcells can be obtained by summing the sensitivities of the subcells (Yoon et al., 2001). This follows from specifying a differential for the production response based on an equal perturbation of each subcell parameter. Further, from (11) it is observed that the time-of-flight sensitivities can be computed for any convex grid cell as long as one is able to trace the streamline to obtain the time-of-flight over the cell. Hence, the

volume of the cell is implicitly accounted for through the time-of-flight over the cell, which is in agreement with the additivity.

A problem with defining sensitivities this way is that small cells will in general have smaller sensitivities, and contrary large cells will in general have larger sensitivities. Thus, smaller modifications will in general be imposed on small cells, and grid effects may therefore occur if there are (large) variations in cell sizes in the underlying unstructured grid. This effect will, to a certain extent, be counteracted by the smoothing regularization if there are other cells with potential for greater modifications in the vicinity of a small cell. One way to remedy these grid effects is to apply rescaled sensitivities defined as the local sensitivity density (sensitivity per area/volume) multiplied by the average cell volume. Since the sensitivities are spatially additive, applying these rescaled sensitivities should therefore give a distribution more equal to the sensitivity distribution obtained on a equisized grid. Another way to remedy the problem is to lump together small cells to larger cells, to get a more uniform grid for the history matching. However, this will in general require some kind of upscaling/downscaling of the reservoir parameters $\mathbf{m}$ and will not be considered herein. We will return to a discussion of grid effects due to variations in cell sizes in the numerical examples below.

4   Generalized Smoothing Stencil

The smoothing operator $\mathbf{L}$ has to be generalized for general unstructured grids. For Cartesian grids the smoothing operator $\mathbf{L}$ was constructed by applying a finite-difference approximation for the Laplacian. More precisely, the well-known five-point and seven-point stencils were used for 2-D and 3-D grids, respectively. Four-point and five-point finite-difference approximations for the Laplacian can also be derived on uniform triangular and tetrahedral grids (Iserles, 1996) (possibly also for non-uniform grids). Equivalent stencils for the Laplacian can also be derived as finite-volume stencils using two-point approximations. These stencils only involve the nearest neighbors and may be less robust because the triangles and tetrahedra have fewer nearest neighbors than the quadrilaterals and hexahedra, respectively. In 3-D, it is sometimes appropriate to use a separate stencil in the z-direction (vertical), because parameters in different layers are usually less correlated. In that way it is possible to match each layer more independently.

All the stencils discussed above can be written on the following general form

$$L_i\, \mathbf{m} \propto \left(\sum_{j \in \mathcal{N}(i)} w_j m_j \right) - w_i m_i, \qquad w_i = \sum_{j \in \mathcal{N}(i)} w_j. \tag{12}$$

Here the neighborhood $\mathcal{N}(i)$ contains other cells sufficiently spatially close that will contribute to the smoothing stencil of a given cell i. Notice that cell i is not included in $\mathcal{N}(i)$.

A naive direct generalization of the finite-difference stencils applied for logically Cartesian grids (using the nearest neighbors) may work fine for grids with quite equisized and equilateral grid cells. However, the generalized stencil will lack robustness and result in grid effects for the smoothing of general unstructured grid that possibly has large variations in cell sizes. On the other hand, the smoothing operator does not necessarily have to accurately approximate the Laplacian; it is most important is that the operator results in a proper smoothing. Indeed, a good smoothing operator for unstructured grids should try to fulfill the following criteria:

(1) The operator should coincide with the five-point (or seven-point) stencil for uniform 2-D (or 3-D) Cartesian grids.
(2) The operator should give the same smoothing effect independently of the local grid density (unless some spatially varying smoothing parameter is incorporated).
(3) The smoothing of each grid cell i should be influenced by an appropriate neighborhood $\mathcal{N}(i)$.
(4) The influence of each neighbor should decay (or stay constant) by the distance $\zeta(i, j)$, and be zero outside some range.
(5) The influence of a neighbor should be bounded as the distance $\zeta(i, j)$ goes to zero.

To meet these criteria, we propose a generalized smoothing stencil on the form

$$w_j = w_{\mathrm{norm}} \cdot \rho(\zeta(i, j); R, \ldots), \quad \text{for } j \in \mathcal{N}(i), \tag{13}$$

where $\mathcal{N}$ is either the radius or k-ring neighborhood, $\rho(\zeta; R, \ldots)$ is a standard correlation function from geostatistics, and w_{norm} is a normalization weight used to ensure that the influence of each neighborhood is approximately the same. The generalized correlation length R is used to control the range of influence for ρ.

4.1 Neighborhood

The k-ring neighborhood $\mathcal{N}_k(i)$ includes all cells that can be reached by k edges or less in the connectivity graph in which the centroids of each cell is a vertex; see Figure 1. The centroids can be precomputed efficiently by decomposing polyhedral cells into triangles/tetrahedra and using area/volume-weighted average of the centroids of the resulting subcells. The 1-ring neighborhood of cell
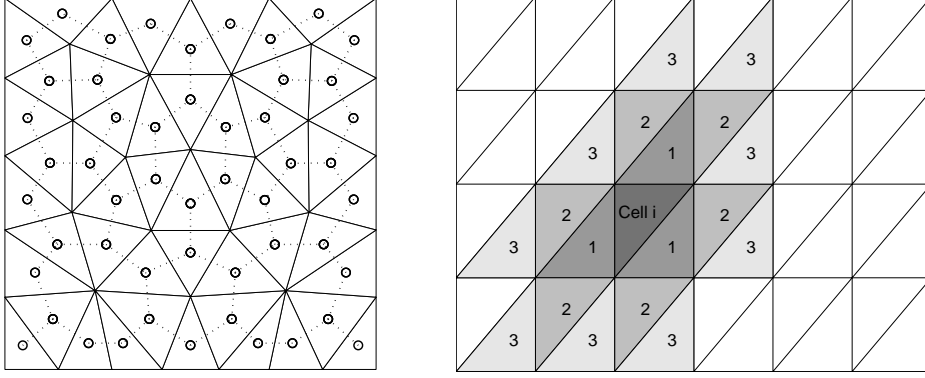
9

Fig. 1. (Left) An example of the connectivity graph, where the centroids of the triangles represent the vertices of the graph. (Right) An example of a k-ring neighborhood $\mathcal{N}_k(i)$ for $k = 1, 2, 3$.

i will be the collection of all cells adjacent to cell i. Figure 1 illustrates the 1-ring, 2-ring, and 3-ring neighborhood for grid cell i in a regular triangular grid. Note that in general $\mathcal{N}_1(i) \subseteq \mathcal{N}_2(i) \subseteq \mathcal{N}_3(i) \subseteq \ldots$. The k-ring neighborhood is sometimes referred to as a kth order neighborhood.

Second, the radius neighborhood, with a radius of x length units, is denoted by $\mathcal{N}_{r=x}(i)$. The radius neighborhood include all (i, j) that are reachable by a search in the connectivity graph without violating $\zeta(i, j) \leq x$. As our distance function, we will use the standard Euclidean distance between the cell centroids. To account for anisotropy, one may alternatively use a non-Euclidean distance measure

$$\zeta_{\mathbf{K}}(i, j) = \|\vec{\zeta}\|_{\mathbf{K}} = \sqrt{\vec{\zeta}^t \mathbf{K} \vec{\zeta}},$$

where $\vec{\zeta}(i, j) = [\zeta_x, \zeta_y, \zeta_z]$ is the vector containing the Euclidean distance in each coordinate direction and $\mathbf{K}$ is positive semi-definite.

Both the k-ring neighborhood and the radius neighborhood give symmetric neighborhood configurations in the sense that if $i \in \mathcal{N}(j)$ then $j \in \mathcal{N}(i)$. For the k-ring neighborhood, the number of cells are bounded so that

$$|\mathcal{N}_k(i)| \leq k \times (\#\text{edges/faces per cell}).$$

The more equisized and equilateral the grid cells are, the closer to the upper bound will in general the number of cells in the k-ring neighborhood be. In general the number of cells in the different k-ring neighborhoods will not vary much over the grid (for a fixed k). On the other hand, for a radius neighborhood the number of cells in a neighborhood can have great variations over the grid. By a proper weighting, we expect the radius neighborhood to give a more robust and less grid-dependent smoothing since the area of

10

influence does not vary much over the grid. Nevertheless, when defining the neighborhood radius one should take some considerations. The radius should be chosen so that the neighborhood of all cells at least includes the nearest neighboring cells, i.e., $\mathcal{N}_1(i) \subseteq \mathcal{N}_{r=x}(i)$. The radius neighborhood will therefore in general have a greater extent, so a smoothing stencil where the weights decay by distance may therefore be reasonable.

For a grid with non-neighboring connections it is not obvious how to define the neighborhood. For instance, close to a fault the grid cells on each side do not necessarily have faces that overlap completely, and consequently a grid cell can have several neighbors with partial overlap of faces. A simple solution is to define the "partial" neighbors as ordinary neighbors. Consequently, the connectivity graph can be defined, and thereby the neighborhood. A more thorough approach would be to in some sense weigh the partial neighbor connections in the stencil. However, in the numerical examples in this paper we will apply the simple approach without weighting.

4.2 Correlation Function

Correlation functions (Abrahamsen, 1997) are used to model the covariance structure of a random spatial quantity and are usually designed to be positive definite by satisfying the following criteria:

$$\rho(0) = 1, \quad |\rho(\zeta)| \leq 1 \; \forall \zeta, \quad \rho(\zeta) \in \mathrm{C}_0 \; \text{for} \; \zeta > 0, \quad \lim_{\zeta \to \infty} \rho(\zeta) = 0. \qquad (14)$$

Positive definiteness is not an issue for our smoothing stencil, and we are therefore free in general to choose from a broader range of functions. However, even though there are higher-order finite-difference stencils for the Laplacian with weights alternating sign based on distance (Iserles, 1996), we will henceforth stick to positive correlation functions. Hence, the first relation in (14) fulfills Requirement 5 above.

A correlation function usually has a parameter R called correlation length or range, which is often considered as the distance ζ for which $\rho \approx 0.05$, i.e., $|\rho(\zeta)| \lesssim 0.05$ for $\zeta > R$. Moreover, some readers may be more familiar with the variogram function $\gamma(\zeta; R)$ than the correlation function, which for stationary Gaussian random fields are given by $\gamma(\zeta; R) = \sigma^2(1 - \rho(\zeta; R))$, where σ^2 is the variance.
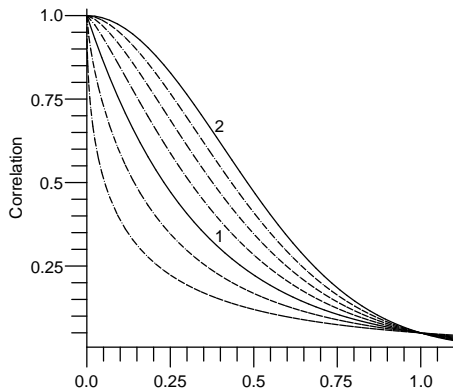
11

Fig. 2. Exponential correlation functions for $R = 1$ plotted as solid curves for $\nu = 1.0, 2.0$ (indicated on plot) and as dashed curves for $\nu = 0.50, 0.75, 1.25, 1.50,$ and 1.75.

In the following we consider either the constant correlation function,

$$\rho_{\mathrm{const}}(\zeta; R) = \begin{cases} 1 \,, & \text{for } 0 \leq \zeta \leq R, \\ 0 \,, & \text{else}, \end{cases}$$

which is discontinuous and thus violates (14), and the exponential correlation function

$$\rho_{\mathrm{exp},\nu}(\zeta; R, \nu) = e^{-3(\zeta/R)^{\nu}}, \qquad 0 < \nu \leq 2,$$

which decays with increasing distance. For $\nu = 2$ the corresponding correlation function is sometimes referred to as the Gaussian correlation function. Figure 2 depicts some exponential correlation functions for different values of the parameter ν. To fulfill Requirement 4 and because positive definiteness is not an issue for our purpose, we set $\rho(\zeta)$ to zero for $\zeta > R$.

In spatial statistics it is common to replace $\left(\frac{\zeta}{R}\right)$ with $\left\| \left[\frac{\zeta_x}{R_x}, \frac{\zeta_y}{R_y}, \frac{\zeta_z}{R_z} \right] \right\|_2$ in the correlation functions ρ to account for anisotropy in the principal coordinate directions. For $R_x = R_y = R_z = R$ the two representations will coincide. If the anisotropy directions are not aligned with the principal directions, a coordinate transformation may be required. This can be performed by measuring ζ through $\| \cdot \|_{\mathbf{K}}$ as described above. Another possibility to account for anisotropy, which is applied in geostatistics, is to construct the correlation function as a product of correlation functions related to different spatial directions, e.g., $\rho(\zeta) = \rho_{xy}(\zeta) \cdot \rho_z(\zeta)$.

12

4.3 Normalization Weights

For w_{norm} we seek a normalization weight such that the influence of each neighborhood is approximately the same. Inspired by Taubin (1995) we therefore propose the following choices:

$$w_{\mathrm{norm}} = \Big(\sum_{j \in \mathcal{N}(i)} \rho(\zeta(i,j)) \Big)^{-1}, \tag{15}$$

$$w_{\mathrm{norm}} = \big(\bar{\rho} \cdot |\mathcal{N}(i)| \big)^{-1}. \tag{16}$$

Here $\bar{\rho}$ is the average correlation over all neighborhoods of the grid:

$$\bar{\rho} = \frac{1}{|\mathcal{G}|\,|\mathcal{N}(i)|} \sum_{i \in \mathcal{G}} \sum_{j \in \mathcal{N}(i)} \rho(\zeta(i,j)).$$

The $\bar{\rho}$ function can be preprocessed or computed when the neighborhoods are traversed. The evaluation of $\bar{\rho}$ only involves arithmetic operations and is thus very fast. Further, since $\bar{\rho}$ can be accumulated, it does not increase the memory requirements.

The weight(15) multiplied by ρ sums to unity for all $j \in \mathcal{N}(i)$ and therefore gives the same weight to all neighborhoods. Further, (16) will also give a normalization on average over all neighborhoods, but (16) adaptively gives more weight to a neighborhood based on the average generalized correlation for the neighborhood. Further, both (16) and (15) will ensure that the total weight given to the smoothing in (4) does not vary much by changing the particular form of the ρ function. We will stick to (16), because it gives an adaptive weighting. Hence, in our weighting operator we have not taken any specific actions to account for boundary effects.

A natural question is if there should be a correspondence between the correlation length in the different directions of the permeability field and the correlation length used in the generalized stencil. In general it should not. The reason is that we assume the basic structure of the permeability field is incorporated into the prior/initial permeability field. The main task of the smoothing stencil is therefore just to preserve the structure by enforcing smooth changes in the inversion process, so the correlation length for the smoothing stencil is therefore more dependent on the grid density. However, it can for instance be advantageous to let the permeabilities change more independently in the different layers, and possibly also on each side of faults. This can partially be incorporated by the approach for anisotropic correlation functions described in Section 4.2. However, the layers and faults are not necessarily aligned with specific coordinate axes. A more advanced generalized correlation function that

incorporates not only the distance function, but also layer information may therefore be required. In other words, spatially varying stencil/neighborhood parameters are required.

For a uniform Cartesian grid, the standard five-point stencil can be represented by our definition by letting the neighborhood be $\mathcal{N}_1$ or $\mathcal{N}_{r=h}$, and w_{norm} be given by either (16) or (15). Further, $\rho(\zeta)$ will have the same value for the different adjacent grid cells for any positive bounded real function. Hence, Requirement 1 can be fulfilled for the generalized smoothing stencil.

In the next section we apply the proposed generalized smoothing stencil to a few numerical examples and discuss its utility.

5   Numerical Examples

For simplicity, we will in the following only focus on 2-D test cases using the simplified flow model for an incompressible, immiscible oil-water system as described in Section 2. First, we compare the performance of the generalized travel-time inversion on uniform Cartesian and uniform triangular grids (Case 1). Second, we investigate the applicability of the generalized travel-time inversion on a non-uniform, highly unstructured triangular grid (Case 2). Finally, we try to apply the generalized stencil to a corner-point grid with faults and non-neighboring connections at the faults (Case 3).

For all cases the flow is described using quadratic relative permeability curves with individually specified end-point mobility ratios. Further, for the forward simulations are performed with a streamline simulator where the pressure solver is a standard two-point flux-approximation (TPFA) scheme for Cartesian grids and a mixed finite-element method (MFEM) for triangular grids. For MFEM we apply the lowest-order Raviart–Thomas basis functions (Raviart and Thomas, 1977). Moreover, for all cases we match synthetic water-cut data obtained from a flow simulation on a reference permeability field. The permeability for each grid cell is treated as an adjustable parameter. Next, starting from an initial (prior) permeability field, we match the water-cut data via the generalized travel-time inversion method.

5.1   Case 1: Cartesian versus Triangular Grid

This synthetic case involves reconstruction of a reference permeability field given on a uniform 21×21 Cartesian grid (see Figure 3) based on the observed water-cut production history from a 9-spot pattern on the Cartesian grid (see
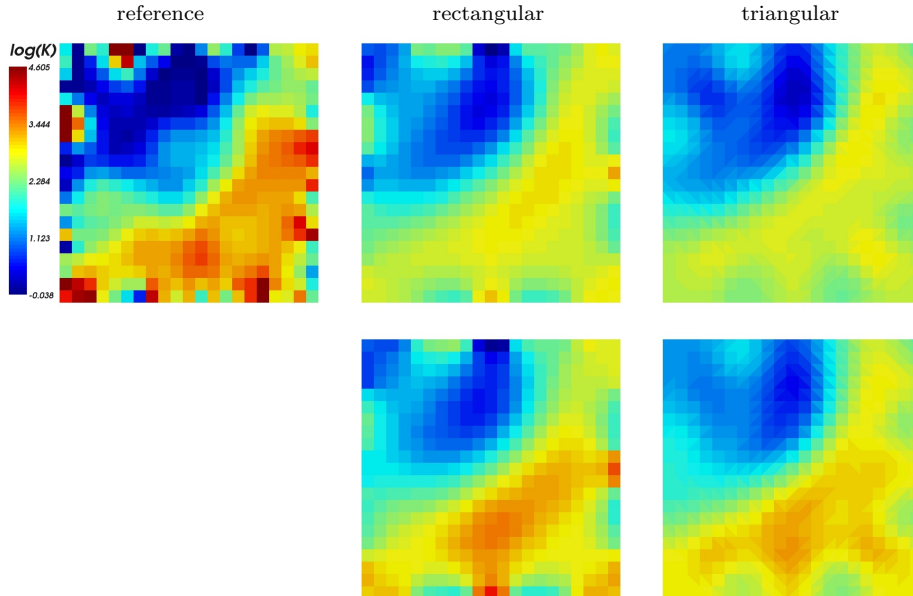
Fig. 3. Case 1: Reference and derived permeability fields on the rectangular grid with Laplacian smoothing and on the triangular grid with smoothing Stencil 3. In the top row $M_{\text{end}} = 0.2$, and in the bottom row $M_{\text{end}} = 10$.

Figure 4) with 5% white noise added. The permeability is reconstructed both on the rectangular grid and on a triangular grid obtained by subdividing each cell in the rectangular grid into two triangles. Hence, the history-matching problem will be more under-determined for the triangular grid, because twice as many parameters have to be matched by the same number of data points (a total of 441 and 882 parameters, respectively).

The dimension of the reservoir is 420×420 meters, and the flow is described by two different end-point mobility ratios, $M_{\text{end}} = 0.2$ and $M_{\text{end}} = 10$. We use a homogeneous permeability as the initial model and apply a standard five-point Laplacian regularization on the rectangular grid. For the triangular grid we apply four different generalized stencils described in Table 1, of which Stencil 1 corresponds with the five-point stencil on the rectangular grid.

The derived permeability fields are shown in Figure 3. Further, Table 1 reports the average discrepancy between the reference and derived permeability field measured by

$$\overline{\Delta \ln K} = \frac{1}{\bar{A}} \sum_{i=1}^{N} A_i |\ln K_i^{\text{ref}} - \ln K_i^{\text{match}}|. \tag{17}$$

Here $\bar{A}$ is the average area for all cells and A_i is the area of cell i. Clearly, the final permeability models capture the large-scale trends of the reference permeability field on both grids. Figure 4 shows a comparison of the initial

Table 1
Case 1: Reduction in percent in residual for time-shift (T) and amplitude (A), and reduction in permeability discrepancy $(\overline{\Delta \ln K})$ on the Cartesian grid with Laplacian smoothing and on the triangular grid with four different stencils.

Strategy	Nbh	ρ	$M_{end} = 0.2$			$M_{end} = 10$		
			T	A	$\overline{\Delta \ln K}$	T	A	$\overline{\Delta \ln K}$
Initial	-	-	100.0	100.0	1.045	100.0	100.0	1.045
Cartesian	-	-	6.8	12.7	0.570	7.5	21.7	0.548
Stencil 1	$\mathcal{N}_1$	ρ_{const}	5.5	13.7	0.614	7.5	23.0	0.599
Stencil 2	$\mathcal{N}_2$	$\rho_{exp,2}$ $(R = 30)$	6.0	13.7	0.601	8.8	23.2	0.590
Stencil 3	$\mathcal{N}_{r=30}$	$\rho_{exp,2}$ $(R = 30)$	6.2	13.6	0.595	9.5	22.9	0.575
Stencil 4	$\mathcal{N}_{r=30}$	$\rho_{exp,2}$ $(R = 50)$	6.5	13.4	0.572	12.0	23.1	0.558
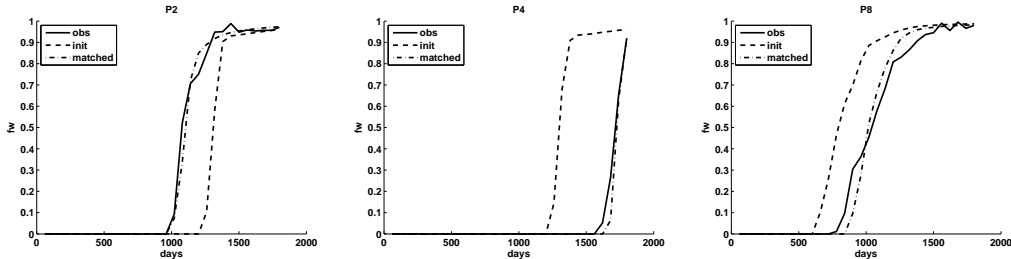
Fig. 4. Case 1: Water-cut curves for Stencil 3 on the triangular grid for producers P2 (North West), P4 (South East), and P8 (East). Mobility ratio $M_{end} = 0.2$.

and final match of the water-cut curves for $M_{end} = 0.2$ for three wells with lowest initial (P2), highest initial (P4), and highest final mismatch (P8) for Stencil 3. Figure 5 shows the reduction in time-shift and amplitude residuals for each iteration using Stencil 3. Further, the reduction in water-cut residuals is also reported in Table 1 for the different stencils. Overall, the match to the production data is quite satisfactory.

The quality of the derived match is similar for all stencils reported in Table 1. The permeability discrepancy is slightly smaller for stencils with radius neighborhood. Conversely, using k-ring neighborhood gives a somewhat lower time-shift residual. A plausible explanation is that the radius neighborhoods usually involve couplings with more distant grid cells, causing the permeability modifications to be more spatially distributed. In other words, more of the modifications occur away from the high sensitivity regions where they would have the greatest impact. This tendency can be controlled by varying the neighborhood radius, the ρ function, and the R parameter.
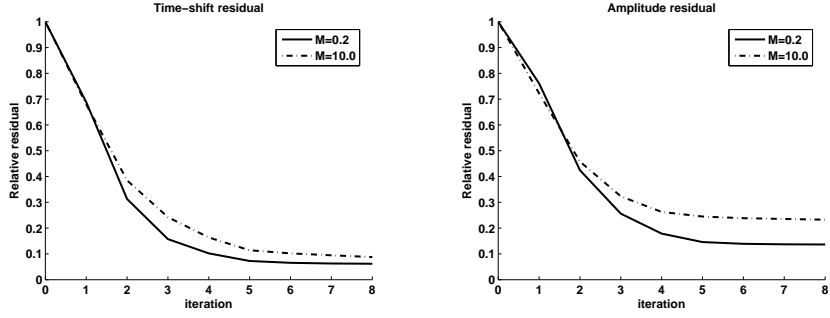
Fig. 5. Case 1: Reduction of residuals for all producers using Stencil 3 for mobility ratios $M_{end} = 0.2$ and $M_{end} = 10$.
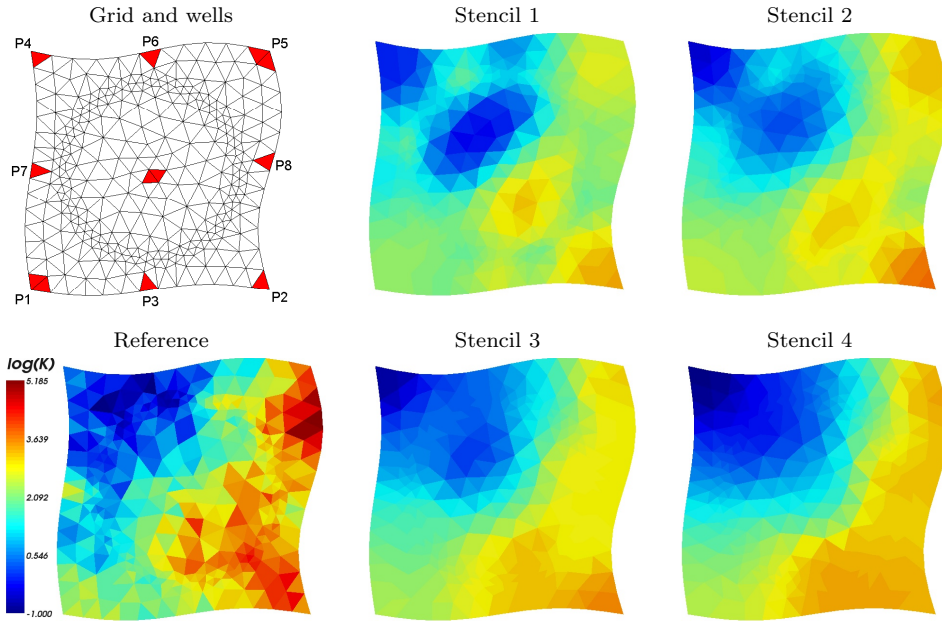

Fig. 6. Case 2: Grid and well-configuration, reference permeability field, and derived permeability fields for Stencils 1 to 4 using sensitivity.

5.2 Case 2: Nine-Spot with a Highly Unstructured Grid

Next we consider the reconstruction of a reference permeability field on an unstructured triangular grid with 581 grid cells. The dimensions of the bounding box for the reservoir is 322×318 meters. Further, the grid is highly unstructured with a ring of high grid density; see Figure 6. This grid is not very realistic for a real reservoir, but was chosen to investigate the effect of varying cell sizes. The initial permeability field for this case is homogeneous with a permeability mean of 7.0 mD. Moreover, the end-point mobility ratio is $M_{end} = 0.5$.

Synthetic production data are obtained by simulating 1200 days of production from a 9-spot pattern (see Figure 7) with 5% white noise added. In the

Table 2
Case 2: Reduction in percent in residual for time-shift (T) and amplitude (A), and reduction in permeability discrepancy $(\overline{\Delta \ln K})$ with four different stencils using sensitivity (Rows 3–6) and rescaled sensitivity (Rows 7–10).

Strategy	Nbh	ρ	T	A	$\overline{\Delta \ln K}$
Initial	-	-	100.0	100.0	1.165
Stencil 1	$\mathcal{N}_1$	ρ_{const}	6.0	14.2	0.771
Stencil 2	$\mathcal{N}_2$	ρ_{const}	8.2	18.9	0.612
Stencil 3	$\mathcal{N}_{r=30}$	ρ_{exp2} $(R = 50)$	9.5	18.6	0.585
Stencil 4	$\mathcal{N}_{r=40}$	ρ_{exp2} $(R = 50)$	12.0	20.9	0.555
Stencil 1	$\mathcal{N}_1$	ρ_{const}	7.0	16.1	0.631
Stencil 2	$\mathcal{N}_2$	ρ_{const}	12.6	22.5	0.525
Stencil 3	$\mathcal{N}_{r=30}$	ρ_{exp2} $(R = 50)$	12.1	20.8	0.546
Stencil 4	$\mathcal{N}_{r=40}$	ρ_{exp2} $(R = 50)$	12.4	21.7	0.568

inversion we only use data from the first 800 days. Data from the remaining 400 days are used to assess the predictive ability of our inversion methods.

Table 2 reports the reduction in time-shift and amplitude residuals for four different stencils and Figure 6 shows the derived permeability fields. All four stencils capture the large-scale trends of the reference permeability, even though the derived permeability fields, especially for the radius neighborhood, are a bit too smooth. This is to be expected since there is no heterogeneity to preserve from the initial (prior) permeability field. As in the previous example, the time-shift residuals are lowest for the k-ring neighborhoods. On the other hand, Stencils 1 and 2 give undesired grid effects inside the ring with small cells, in which the initial homogeneous permeability field is still visible, in particular for Stencil 1 in the quadrant bounded by the injector and wells P6, P4 and P4. Stencils 3 and 4 are more able to capture the large-scale permeability structures, as seen in Figure 6 and from the permeability discrepancy. However, small artifact are also visible for these stencils, especially for Stencil 3. Without smoothing, small cells with small sensitivity will in general get smaller modifications than larger cells. However, the smoothing will tend to distribute the modifications. For the 1- and 2-ring neighborhoods, the stencils were not able to span over the ring with small cells and therefore resulted in too small modifications in this high-density band. For the radius neighborhood, on the other hand, the region of influence crosses over the high-density band and therefore distributed the modifications more properly.

Figure 7 shows a comparison of the initial and final match of the water-cuts for Stencil 4. The overall match to the production data is satisfactory, and
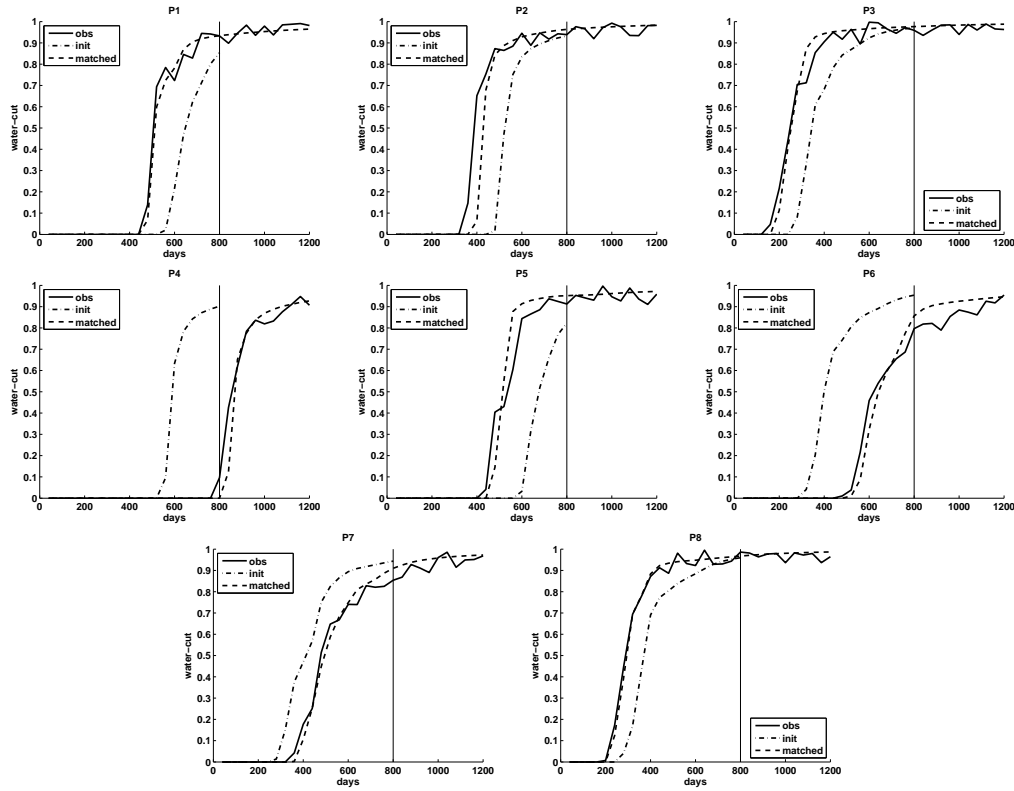
Fig. 7. Case 2: Water-cut match for Stencil 4 for the wells P1–P8. The time span 0–800 days is the matching period, while the time span 800–1200 days is prediction.
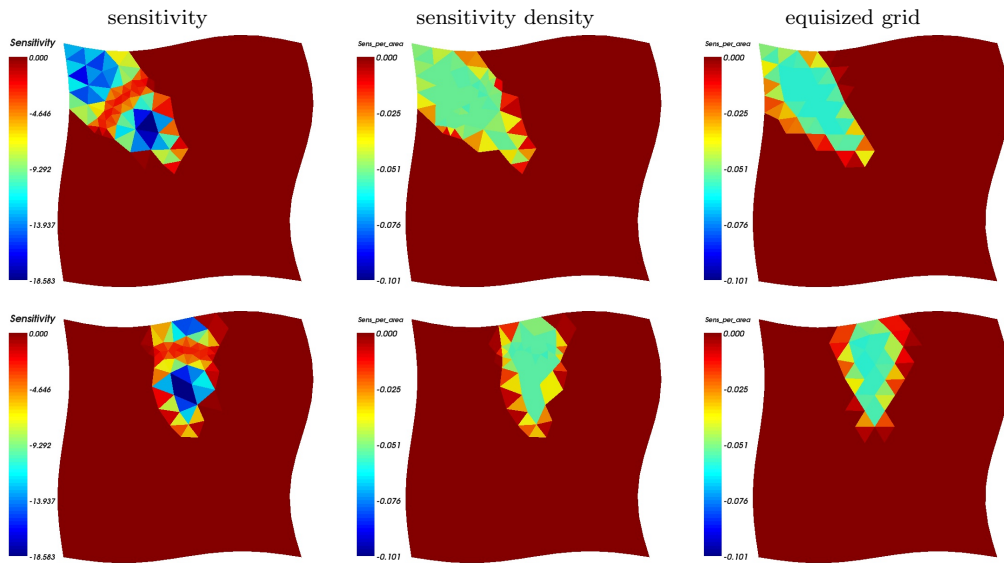

Fig. 8. Case 2: Time-shift sensitivity and sensitivity density (not rescaled) computed for a homogeneous permeability field for wells P4 (top) and P6 (bottom).

the prediction in the period from 800 to 1200 days shows good agreement. In particular, the prediction for well P4 is good, given that this well had almost no significant water responses during the matching period.
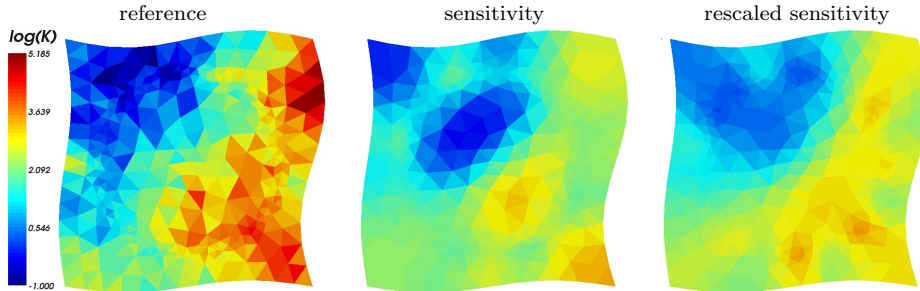
Fig. 9. Case 2: Permeability field derived using Stencil 1 with sensitivity and rescaled sensitivity.

In Section 3.2 we proposed to use rescaled sensitivities rather than sensitivities in the inversion process to counteract effects from heterogeneous cell sizes. The rescaled sensitivity of a cell i is computed by $G_i \bar{V} / V_i$, where G_i is the sensitivity and V_i is the volume for cell i and $\bar{V}$ is the average volume of all cells. Figure 8 shows sensitivities G_i and sensitivity densities G_i/V_i for wells P4 and P6. As expected, the sensitivities for small cells are in general smaller than for large cells. The sensitivity densities, on the other hand, do not show any grid effects and are similar to those computed on an (almost) equisized grid. However, as seen in Figure 8, the sensitivities and sensitivity densities are of different magnitude. We therefore suggest to multiply the sensitivity densities by the average volume of all cells $\bar{V}$ to obtain what we will refer to as rescaled sensitivities. Hence, the sensitivities and the rescaled sensitivities will be more of the same magnitude and will coincide on uniform grids. The drawback with using rescaled sensitivities is that it might be harder to match the data, because rescaled sensitivities will enforce greater modifications in cells that are less important with respect to shifting the production curves (less sensitivity).

Figure 9 shows a comparison of the derived permeabilities for Stencil 1 using sensitivities and rescaled sensitivities, respectively. The resulting permeability field applying the rescaled sensitivities does not show indications of grid effects from the high-density band. Further, Table 2 shows the reduction in residuals and average permeability discrepancies for both applying the sensitivities and the rescaled sensitivities for different stencils. The permeability discrepancies seems to improve by applying rescaled sensitivities. Especially the k-ring stencils seem to improve the quality of the derived permeability fields. Even so, the reduction in the residuals is in general slightly degraded, as expected.

To test the robustness of the generalized stencil, the neighborhood, and the application of rescaled sensitivities, we have systematically performed the inversion for different stencil parameters for the stencil $(\rho_{\exp2}, \mathcal{N}_{r=x})$. The results are presented in three 7×7 test matrices with the correlation length R and the neighborhood radius r as parameters. The correlation length takes the values $R \in \{20, 30, 40, 50, 60, 70, \infty\}$, while the the neighborhood radius takes
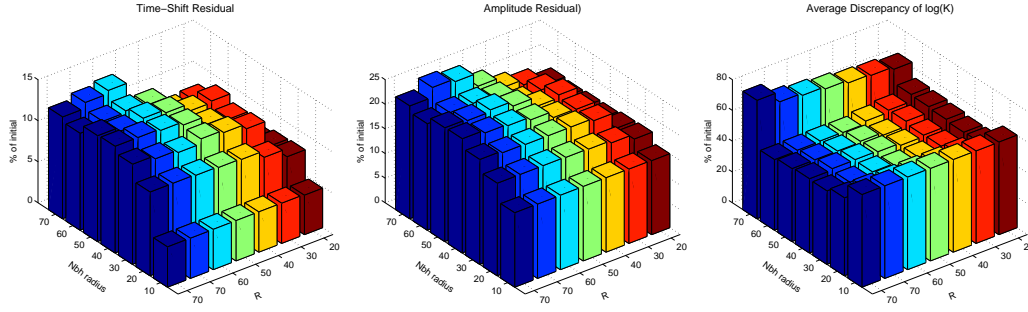
Fig. 10. Case 2: Robustness of stencil parameter R and neighborhood radius r.
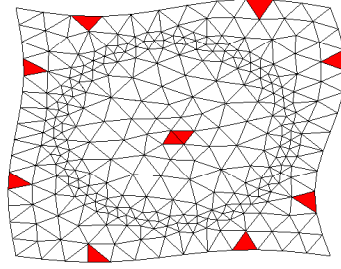

Fig. 11. Case 2: Altered well-configuration.

the values $r \in \{10, 20, 30, 40, 50, 60, 70\}$; both measured in meters. Hence, by letting R go to infinity the exponential correlation function will approach the constant correlation function. Figure 10 shows the reduction of time-shift and amplitude residuals after eight iterations, as well as the average discrepancy between matched and reference permeability fields. Judging from the residual plots, it seems like the more weight is given to the smoothing stencil away from the center cell, the harder it is to match the data. In other words, more of the modifications are made away from where they would have the greatest impact on the simulated production responses. Even so, the quality of the match is not degraded considerably. The permeability discrepancy is very robust with respect to the smoothing parameters. There seems to be a lower and upper limit for the stability region with respect to the neighborhood extent, but the radius of the stable region is quite large given the dimension of the reservoir.

Finally, we test the predictive abilities of the derived permeability fields for the altered well-configuration shown in Figure 11. Table 3 reports the reduction in amplitude and time-shift residuals compared with a simulation using the prior homogeneous model. Here the best results, by far, are obtained using the radius neighborhood.

5.3 Case 3: Faulted Corner-Point Grid

We consider a 2-D corner-point reservoir model with diagonal permeability streaks, dynamic well configuration and non-sealing faults that induce non-

21

Table 3
Case 2: Reduction in percent for misfit in time-shift (T) and amplitude (A) by applying the derived permeability fields for the altered well-configuration.

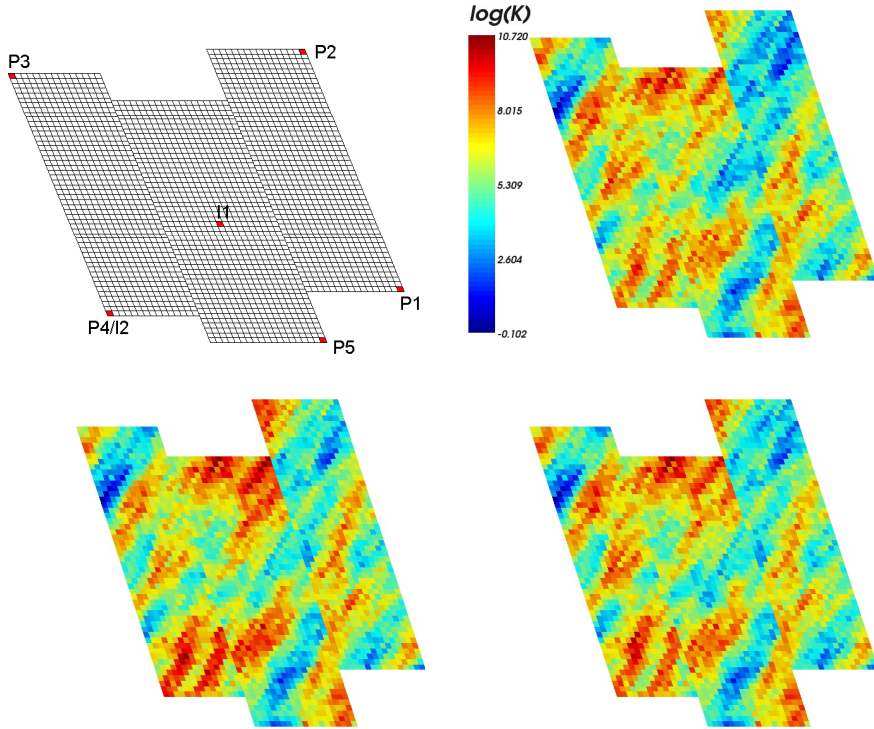| Strategy	Nbh	ρ	T	A
Initial	-	-	100.0	100.0
Stencil 1	$\mathcal{N}_1$	ρ_{const}	47.1	50.4
Stencil 2	$\mathcal{N}_2$	ρ_{const}	33.4	38.3
Stencil 3	$\mathcal{N}_{r=30}$	$\rho_{\text{exp2}}\ (R = 50)$	27.8	33.0
Stencil 4	$\mathcal{N}_{r=40}$	$\rho_{\text{exp2}}\ (R = 50)$	27.0	32.0

Fig. 12. Case 3: Grid and well-configuration (upper left), reference permeability field (upper right), initial (prior) permeability field (lower left) and derived permeability field by Stencil 3 (lower right).

neighboring connections; see Figure 12. The lognormal permeability field has a 50×50 logical structure, but because of the faults, the grid has three shifted sections. Further, the dimensions of bounding box for the reservoir is 646×605 meters, and the end-point mobility ratio is $M_{\text{end}} = 0.5$.

The history-matching will be performed on the corner-point grid, but to be able to trace streamlines over the non-neighboring connections, we simulate the flow on a triangular grid where we have subdivided each corner-point cell into two triangles and in addition refined the grid by triangles close to the
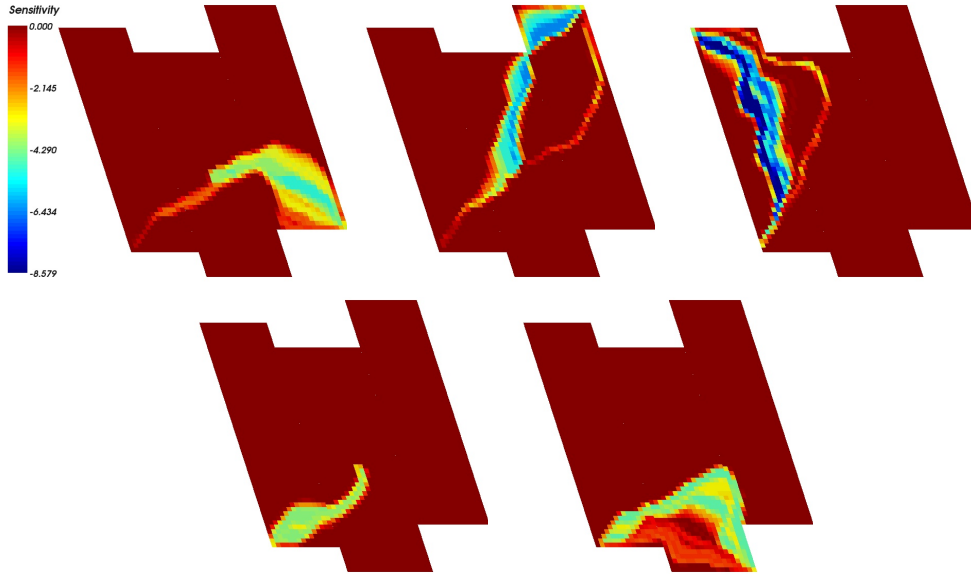
Fig. 13. Case 3: Time-shift sensitivities for the five producers.

faults to obtain a matching grid. Hence, no upscaling/downscaling is required between the simulation grid and the history-matching grid because the permeability field originally is given on the coarsest grid. For each forward simulation we use a pressure steps of 100 days. In Section 4.1 we discussed how to handle the non-matching cell faces at the faults when defining the neighborhood.

Synthetic production data were generated by adding 15% white noise to the water-cut curves computed from the reference permeability. Initially, the well-configuration is a kind of five-spot configuration, with an injector in the center and four producers in the corners; see Figure 12. Further, the producers operate at equal constant rate. Producer P4 in the south-west corner has an early breakthrough and is therefore converted to an injector after 900 days. Simultaneously, a new producer (P5) is introduced in the lower-left corner of the section in the middle (south). This part of the reservoir has not been depleted at all yet. The new injector is injecting 3/5 of the total injection rate. The motivation for the updated well-configuration is also to introduce an additional sweep from the south-west corner. After the well conversion, all producers operate at constant equal rate. The updated well-configuration is kept throughout the rest of the production period. Thus, we wish to integrate 2500 days of production data from five producers in total.

To match observed data, we start from the prior permeability field shown in Figure 12 and treat the permeability in each corner-point cell as an adjustable parameter, giving a total of 2500 unknown parameters to be estimated. The corner-point sensitivities are obtained by summing the sub-cell sensitivities; see Figure 13. Table 4 reports the reduction in residuals with respect to time-shift and amplitude. The resulting permeability field for Stencil 3 after eight

23

Table 4

Case 3: Reduction in percent for misfit in time-shift (T) and amplitude (A), and reduction in average discrepancy in log permeability $\overline{\Delta \ln K}$).

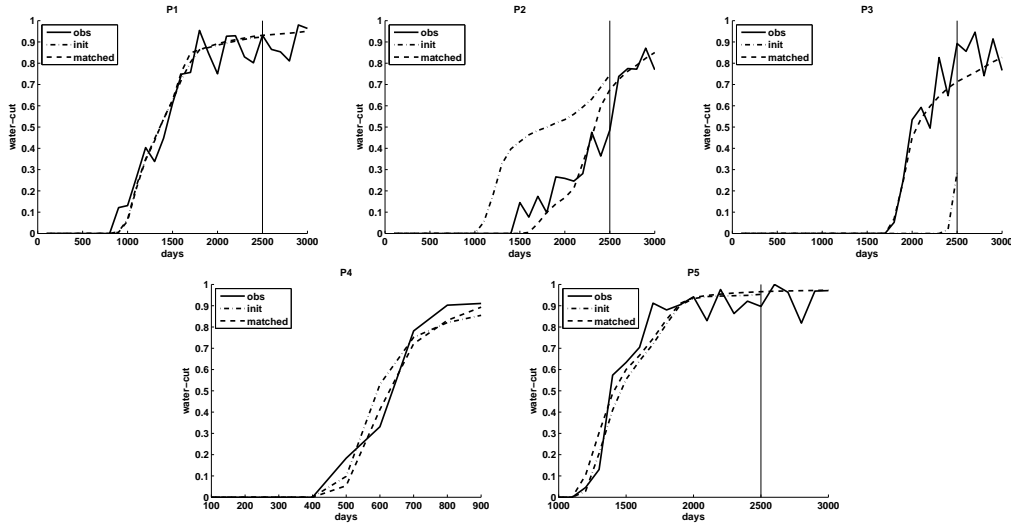| Strategy	Nbh	ρ	T	A	$\overline{\Delta \ln K}$
Initial	-	-	100.0	100.0	0.421
Stencil 1	$\mathcal{N}_1$	ρ_{const}	5.5	35.0	0.334
Stencil 2	$\mathcal{N}_2$	ρ_{const}	4.9	35.0	0.332
Stencil 3	$\mathcal{N}_{r=30}$	ρ_{exp2} $(R = 50)$	5.8	35.2	0.334
Stencil 4	$\mathcal{N}_{r=40}$	ρ_{exp2} $(R = 50)$	5.7	35.8	0.332

Fig. 14. Case 3: Water-cut match for the Stencil 3 for wells P1–P5. The time span 0–2500 days is the matching period, while the time span 2500–3000 days is prediction.

iterations is shown in Figure 12. The updated permeability field is in general closer to the reference, and the realism of the permeability field is not degraded by the history matching. This is also confirmed by the average permeability discrepancies in Table 4. In the derived permeability fields there was no indications of smearing across the faults. This is caused by the regularization that keeps the modifications small and smooth, and the localization of the sensitivities; see Figure 13. Figure 14 shows a comparison of the initial and the final match of the water-cut curves for the production wells obtained with Stencil 3. Overall, the match to the production data and the quality of the derived permeability fields are satisfactory.

Concluding Remarks

The generalized travel-time method for inversion of production data has been successfully applied to unstructured grids. For equisized grids, the original framework developed previously by Vasco et al. (1999) and He et al. (2002) can be applied almost directly, as has previously been done for grids that are logically Cartesian and quite uniform. For general unstructured grids that may have (large) differences in cell sizes and in the number of connections, our investigations revealed that a generalized smoothing operator should be introduced to obtain a good match. Our new smoothing stencils introduce a few extra regularization parameters, but the inversion is robust to these parameter values and it is easy to make a good choice by considering the cell sizes of the grid.

Similarly, we found that rescaled sensitivities should be incorporated to give permeability fields without undesired heterogeneities induced by grid effects. The magnitude of potential modifications of the reservoir parameters are determined by the sensitivities and data misfits. Since small grid cells generally have smaller sensitivities than larger cells, the magnitude of the induced parameter modifications will depend on heterogeneity of the grid. Because the production-response sensitivities are spatially additive, it will often be better to use rescaled sensitivities instead of sensitivities in the inversion to obtain realistic modifications, even though this can make it slightly harder to match the observed data. For uniform grids the sensitivities and the rescaled sensitivities will coincide.

In the current paper we have only investigated two-dimensional numerical examples, including non-neighboring connections. This is partly because 2-D examples are well suited for visualization and for detecting the principal effects. Real 3-D reservoir models are, of course, much more challenging. Although the framework we have proposed for applying the generalized travel-time inversion on general unstructured grids is general and should apply to 3-D grids as well, additional effects like layering and various grid-degeneracies may prove important in 3-D. Extensions to real-life 3-D models is therefore a topic of future research.

Acknowledgments

References

Aarnes, J. E., 2004. On the use of a mixed multiscale finite element method for greater flexibility and increased speed or improved accuracy in reservoir simulation. Multiscale Model. Simul. 2 (3), 421–439.

Aarnes, J. E., Krogstad, S., Lie, K.-A., to appear. Multiscale mixed/mimetic methods on corner-point grids. Comput. Geosci.

Abrahamsen, P., 1997. A review of Gaussian random fields and correlation functions, second edition. Tech. Rep. 917, Norwegian Computing Center, Oslo, Norway.

Chen, A., Hou, T., 2002. A mixed multiscale finite element method for elliptic problems with oscillating coefficients. Math. Comp. 72 (242), 541–576.

Cheng, H., Datta-Gupta, A., He, Z., 2005a. A comparison of travel-time and amplitude matching for field-scale production-data integration: Sensitivity, nonlinearity, and practical implications. SPE J. 10 (1), 75–90.

Cheng, H., Kharghoria, A., He, Z., Datta-Gupta, A., 2005b. Fast history matching of finite-difference models using streamline-derived sensitivities. SPE Reserv. Eval. Eng. 8 (5), 426–436.

He, Z., Yoon, S., Datta-Gupta, A., 2002. Streamline-based productoin data integration with gravity and changing field conditions. SPE J. 7 (4), 423–436.

Hohl, D., Jimenez, E., Datta-Gupta, A., 24–27 September 2006. Field experiences with history matching an offshore turbiditic reservoir using inverse modeling. In: SPE Annual Technical Conference and Exhibition. San Antonio, TX, USA, SPE 101983.

Iserles, A., 1996. A First Course in the Numerical Analysis of Differential Equations. Cambridge University Press.

Paige, C., Saunders, M., 1982. LSQR: An algorithm for sparse linear equations and sparse least squares. ACM Transactions on Mathematical Software 8 (1), 43.

Qassab, H., R, M. K., Pavlas, Afaleg, N., Ali, H., Kharghoria, A., He, Z., Lee, S., Datta-Gupta, A., 5–8 October 2003. Streamline-based production data integration under realistic field conditions: Experience in a giant Middle-Eastern reservoir. In: SPE Annual Technical Conference and Exhibition. Denver, Colorado, USA, SPE 84079.

Raviart, P.-A., Thomas, J., 1977. A mixed finite element method for 2nd order elliptic problems. Mathematical Aspects of Finite Element Methods (Proc. Conf., Consiglio Naz. Delle Ricerche (C.N.R), Rome, 1975), Lecture Notes in Mathematics, Springer, Berlin 606, 292–315.

Stenerud, V., Kippe, V., Lie, K.-A., Datta-Gupta, A., submitted. Multiscale-streamline simulation and dynamic data integration for high-resolution subsurface models. Water Resources Research.

Stenerud, V., Kippe, V., Lie, K.-A., Datta-Gupta, A., to appear. Adaptive multiscale streamline simulation and inversion for high-resolution geomodels. SPE J.

Taubin, G., 6–11 August 1995. A signal processing approach to fair surface design. In: SIGGRAPH 95 Conference Proceedings. Los Angeles, California, USA, pp. 351–358.

Vasco, D., Yoon, S., Datta-Gupta, A., 1999. Integrating dynamic data into high-resolution models using streamline-based analytic sensitivity coefficients. SPE J. 4 (4), 389–399.

Yoon, S., Malallah, A., Datta-Gupta, A., Vasco, D., Behrens, R., 2001. A multiscale approach to production-data integration using streamline models. SPE J. 6 (2), 182–192.